Energy & Environmental Science

Reconfiguring Zn Deposition Dynamics via Epitaxial Zn2+ Pathway in Profiled Viscose Rayon for Long-Cyclability Zinc-Ion Batteries

Journal:	*Energy & Environmental Science*
Manuscript ID	EE-ART-01-2025-000052.R1
Article Type:	Paper
Date Submitted by the Author:	30-Mar-2025
Complete List of Authors:	Ou, Sainan; Fujian Agriculture and Forestry University Zheng, Jiaxian; Fujian Agriculture and Forestry University Chen, Xingshu; Fujian Agriculture and Forestry University Li, Ran; Fujian Agriculture and Forestry University Yuan, Zhanhui; Fujian Agriculture and Forestry University, Liu, Shude; Donghua University; Yonsei University, Mechanical Enginering ; Nagoya University, Niu, Yao; Fujian Agriculture and Forestry University An, Meng; The University of Tokyo, Department of Mechanical Engineering; The University of Tokyo Zhou, Ge; Sichuan University Yamauchi, Yusuke; University of Queensland, Chemical Engineering; Nagoya University, Zhang, Xinxiang; Fujian Agriculture and Forestry University,

Broader context

Rechargeable aqueous zinc-ion batteries (AZIBs) are promising candidates for stationary energy storage due to their intrinsic safety, environmental sustainability, and cost-effectiveness. However, AZIBs are still facing great challenges including uncontrollable dendrite formation and hydrogen evolution reaction (HER) at Zn anode. To date, various strategies have been proposed to tackle the above issues, including electrolyte composition adjustment, regulation of Zn electrodes, and separator modification. Among them, separator modification provides a more straightforward and highly effective strategy for mitigating dendrite growth and facilitating desolvation of hydrated Zn^{2+}. Nevertheless, the complex and costly synthesis processes involved in the separator modification hinder their practical application. We address this bottleneck by screening inexpensive commercial viscose fabrics, derived from profiled viscose rayons, to be used as separator directly. Profiled viscose rayons with surface grooves and abundant carboxyl groups show excellent ability in reconfiguring Zn deposition dynamics of AZIBs for achieving long cycle, providing a promising strategy for separator design to induce uniform growth of Zn crystals along the (002) plane.

ARTICLE

Reconfiguring Zn Deposition Dynamics via Epitaxial Zn^{2+} Pathway in Profiled Viscose Rayon for Long-Cyclability Zinc-Ion Batteries

Received 00th January 2025,
Accepted 00th January 2025

DOI: 10.1039/x0xx00000x

Sainan Ou,[a,†] Jiaxian Zheng,[a,†] Xingshu Chen,[a] Ran Li,[a] Zhanhui Yuan,*[a] Shude Liu,*[b] Yao Niu,[c] Meng An,*[d] Ge Zhou,[e] Yusuke Yamauchi,[f,g] Xinxiang Zhang*[a]

Rechargeable aqueous zinc-ion batteries (AZIBs) are promising candidates for stationary energy storage due to their intrinsic safety, environmental sustainability, and cost-effectiveness. However, their cycling stability is hammered by uncontrollable dendrite formation and hydrogen evolution reaction (HER) at Zn anode. Here, we propose a cost-effective commercial viscose fabric, derived from profiled viscose rayons, as a versatile separator for reconfiguring the interface dynamics of Zn deposition, enabled by the surface grooves with abundant carboxyl groups on profiled viscose rayons. Results show that carboxyl groups facilitate the desolvation of hydrated Zn^{2+} to suppress HER while surface grooves provide epitaxial Zn^{2+} pathways for rapid horizontal transport of Zn^{2+} on the surface of Zn anode which promotes the transition of Zn deposition manner from 2D to 3D diffusion and hence regulates the grow direction of Zn crystals from (101) to (002) to form a uniform and dense Zn deposition on anode. Consequently, AZIBs implementing the viscose fabric separator exhibit high battery performance, including improved cycle life over 4600 h at 1 mA cm^{-2} and enhanced rate capability. This work highlights the significant potential of profiled viscose rayon in reconfiguring the interface dynamics of Zn deposition, providing guidance for the design of advanced separators in AZIBs.

Introduction

Aqueous zinc-ion batteries (AZIBs) have been recognized as a promising alternative to lithium-ion batteries, attributed to their high safety without flammability, abundant reserves of Zn, low cost and environmental benignity.[1-3] However, Zn anodes still suffer from uncontrollable dendrite growth and hydrogen evolution reaction (HER) due to the unstable electrode/electrolyte interface, which hinders the reversibility of Zn plating/stripping and deteriorates the cycling lifespan of AZIBs.[4-6] To this end, various strategies have been proposed to tackle the above issues, including electrolyte composition adjustment,[7-9] regulation of Zn electrodes,[10-12] and separator modification.[13-15] Among them, separator modification provides a more straightforward and highly effective strategy for mitigating dendrite growth and facilitating desolvation of hydrated Zn^{2+},[16] thereby addressing the intrinsic causes of short circuits and performance degradation associated with dendritic formation and HER. To date, various modification strategies have been employed to functionalize GF separators,[17-19] filter paper separators,[20, 21] natural polymer separators,[22-26] synthetic polymer separators[27-30] and other separators[31-34] for reconfiguring Zn deposition dynamics in the interface of electrolyte/Zn anode for uniform Zn deposition. Nevertheless, the complex and costly synthesis processes involved in the separator modification hinder their practical application.[17, 24, 35, 36]

For the commercialization of AZIBs, it is a good choice to screen inexpensive commercial films or fabrics to be used as separators directly. Building on this rationale and leveraging our academic expertise, ultra-low-cost commercial viscose fabric (VF) made from profiled viscose rayons emerges as a promising separator material. Profiled viscose rayon is characterized by its notable flexibility and the presence of abundant carboxyl groups,[37, 38] which can modulate the solvation structure. Moreover, the profiled viscose rayon features a petal-like cross-section and numerous longitudinal grooves on its surface,[39] the spontaneous capillary action may drive the rapid transport of Zn^{2+} within the surface grooves. Current researchers generally believe that coordination of Zn^{2+} with functional groups (amino, sulfonic acid, and carboxyl groups, etc.) introduced during the modification of the separator builds Zn^{2+} channels,[40] thereby accelerating the transport of Zn^{2+}, which is very important for

[a]College of Materials Engineering, Fujian Agriculture and Forestry University, Fuzhou, 350108, China
E-mail: zhanhuiyuan@fafu.edu.cn (Z. Yuan); xxzhang0106@fafu.edu.cn (X. Zhang)
[b]Engineering Research Center of Technical Textiles, Ministry of Education, College of Textiles, Donghua University, Shanghai, 201620, China
E-mail: sdliu@dhu.edu.cn
[c]College of Mechanical and Electrical Engineering, Shaanxi University of Science and Technology, Xi'an, 710021, China
[d]Department of Mechanical Engineering, The University of Tokyo, 7-3-1 Hongo, Bunkyo, Tokyo 113-8656, Japan
E-mail: anmeng@photon.t.u-tokyo.ac.jp (M. An)
[e]College of Chemistry, Sichuan University, Chengdu, 610040, China
[f]School of Chemical Engineering and Australian Institute for Bioengineering and Nanotechnology (AIBN), The University of Queensland, Brisbane, QLD 4072, Australia
[g]Departent of Materials Process Engineering, Graduate School of Engineering, Nagoya University, Nagoya 464-8603, Japan
†These authors contribute to this work equally.
Supplementary Information available: [details of any supplementary information available should be included here]. See DOI: 10.1039/x0xx00000x

reconfiguring Zn deposition dynamics. As VF is used as a separator for AZIBs, most profiled viscose rayons are parallel to the Zn anode, indicating that profiled viscose rayons would provide amounts of pathways for rapid horizontal transport of Zn^{2+} at the electrolyte/anode interface. This would allow the VF separator to remove the tip effect on the microscopically uneven Zn anode, as Zn^{2+} aggregated due to the tip effect would be quickly transported horizontally to the Zn-deficient areas also formed by the tip effect, thereby achieving a very uniform distribution of Zn^{2+} on the surface of the Zn anode and an ultra-short 2D diffusion during Zn deposition. In addition, the coordination of carboxyl groups on profiled viscose rayon with Zn^{2+} may promote the desolvation of hydrate Zn^{2+},[41] thereby preventing water from reaching the surface of Zn anode for inhibiting HER.[42] Therefore, the research on VF separator composed of profiled viscose rayon will provide new insights into Zn deposition dynamics reconfigured by separators.

In this work, we demonstrate that profiled viscose rayon in VF separator with surface grooves and polar carboxyl groups enables highly reversible Zn plating/stripping of AZIBs. To elucidate the underlying mechanism of profiled viscose rayon in reconfiguring Zn deposition dynamics, validation experiments and computational simulation are designed and implemented to explain how profiled viscose rayon regulates the deposition behavior of Zn^{2+} and enhances the electrochemical performance of AZIBs. The most interesting finding is that the surface grooves on profiled viscose rayon serve as epitaxial Zn^{2+} pathways for rapid horizontal transport of Zn^{2+} on the surface of Zn anode which promotes the transition of Zn deposition manner from 2D to 3D diffusion, endowing the VF separator with excellent ability to regulate the grow direction of Zn crystals from (101) to (002) and form a uniform and dense Zn deposition on anode. Zn deposition dynamics of these physical Zn^{2+} transport pathways (surface grooves) within the profiled viscose rayon of VF separator are fundamentally distinct from the hypothetical virtual pathways formed by the functional groups in the reported functionalized separators. Therefore, VF separator endows AZIBs with ultra-long cycle stability while providing an extremely low-cost material solution. As a result, Zn||Cu half-cells with the VF separator exhibit reversible Zn plating/stripping for 500 cycles with an average Coulombic efficiency (CE) of 99.36%. Furthermore, Zn||Zn symmetric cells with the VF separator demonstrate an ultra-durable lifetime of over 4600 h at an area capacity of 1 mAh cm^{-2}. Additionally, this work highlights the significant potential of profiled viscose rayon in reconfiguring the interface dynamics of Zn deposition, providing the guidance for the design of advanced separators in AZIBs.

Results and Discussion

Three types of commercial spunlaced non-woven fabrics, including viscose fabric (VF), cotton fabric (CF), and blended fabric (BF) from 50% viscose rayon and 50% polyester rayon were selected as separators for AZIBs, which are compared with traditional separators of glass fiber (GF) and filter paper (FP). Figure 1a shows that all separators are stacked randomly from individual fibers and there are amounts of inter-fiber pores for electrolyte uptake. The comparison of the physical properties of these separators, including electrolyte affinity (Figure S1), electrolyte uptake (Figure S2), and tensile strength (Figure S3), indicates that CF and VF are good candidates as separators of AZIBs. To evaluate the effect of separators on the cycle stability, Zn symmetric cells equipped with GF, FP, CF, BF and VF separators were assembled and subjected to galvanostatic cycling tests. These separators are all made of fibers with diameters ranging from 1 to 30 μm (Figure 1a and Figure S4). Their loose and porous characteristics require a large thickness to realize the cycling of Zn symmetric cells. Therefore, the commercial GF separator is quite thick (675 μm as shown in Figure S5) and its symmetric cell is short-circuited after cycling for only 52 h at 1 mA cm^{-2} with a capacity of 1 mAh cm^{-2} (Figure 1b). The FP, CF, and BF separators, with thicknesses ranging from 200 to 260 μm (Figure S5), struggle to achieve stable cycling, with cycling lifespans of only 22 h, 7 h, and 2 h, respectively. However, surprisingly, despite the VF separator having a similar thickness (Figure S5) and fiber aggregation structure (Figure S4) as CF and BF, it endows the symmetric cell with an ultra-long cycling lifetime of 4600 h (Figure 1b). It should be noted that the symmetric cell with a VF separator exhibits higher voltage hysteresis than the others. The phenomenon is mainly attributed to the smaller critical Zn nucleus radius during the initial deposition stage, which leads to the formation of finer-grained Zn deposits.[43, 44] The effect of separators on cycling stability at higher current density and capacity is also tested (Figure S6-S10). Encouragingly, the VF separator also endows cells with good cycling stability under harsher conditions, cycling for approximately 1180 h at 2 mA cm^{-2} with a capacity of 4 mAh cm^{-2} and 620 h at 4 mA cm^{-2} with a capacity of 4 mAh cm^{-2}, respectively. In addition, the first-cycle Coulombic efficiency of Zn||Cu half-cell employing the VF separator (86.56%) is higher compared to cells using GF (70.48%), FP (85.2%), CF (82.69%), and BF (85.55%) separators (Figure S11). Moreover, the half-cell with VF separator also shows a high average CE of 99.36% over 500 cycles, while the half-cells with other separators exhibit significant voltage fluctuations within 150 cycles (Figure 1c), indicating that VF separator enhances the Zn plating/stripping reversibility.

It is well-known that the cycling stability and CE of AZIBs are severely compromised by the formation of dendrites and HER on the surface of Zn anode. [45] Among these five separators, VF and CF separators attract our great attention, as profiled viscose rayon is regenerated from plant fibers, such as cotton fiber. The above discussion indicates that the regeneration process of cotton fiber into viscose rayon endows VF-equipped cells with excellent cycling stability. In-depth research into the impact of VF and CF separators is crucial for understanding the mechanism by which VF regulates Zn deposition and suppresses HER. Meanwhile, commercial GF separator is also studied as a control. Therefore, Zn symmetric

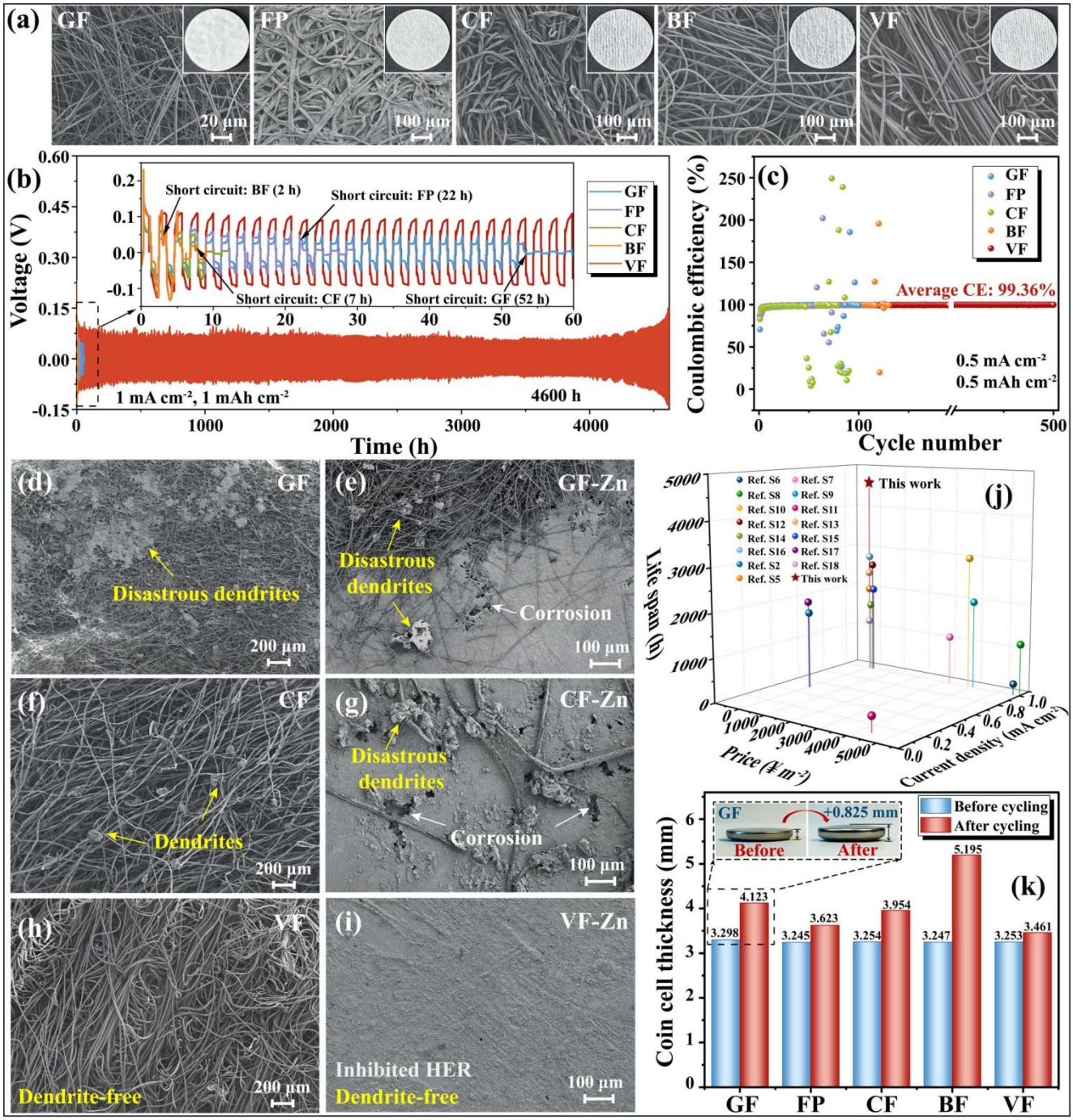

Figure 1. (a) SEM images and photos of various separators. (b) Cycling performance of the symmetric cells with various separators at 1 mA cm^{-2} for 1 mAh cm^{-2}. (c) Coulombic efficiency of Cu||Zn asymmetry cells at 0.5 mA cm^{-2}. SEM images of separators (d, f, h) and Zn anodes (e, g, i) of symmetric cells with GF, CF and VF separators cycled for 40 cycles at 1 mA cm^{-2} for 1 mAh cm^{-2}. (j) Comparison of this work with the reported works. (k) Cell thickness before and after cycling with different separators.

cells with GF, CF and VF separators are cycled for 40 cycles (about 100 h) at 1 mA cm^{-2}, which are disassembled for SEM characterization of the cycled separators and anodes (Figure 1d-i). As shown in Figure S12a-b and Video S1, when the battery is disassembled, separating the GF and CF separators from the electrodes proves to be extremely difficult. GF separator is torn and many GF fibers are adhered onto the Zn electrode due to its poor wet tensile strength (Figure S3b) and severe penetration of Zn dendrites into it (Figure 1d, e). CF separator acts like a double-sided adhesive tape, holding two electrodes tightly together owing to its good tensile strength (Figure S3a-c) and also the penetration of Zn dendrites into the CF separator (Figure 1f). Surprisingly, the cycled Zn electrode can be easily pushed horizontally away from the VF separator (Figure S12c and Video S1), indicating that there is no binding between them because no dendrite has penetrated the VF separator (Figure 1h). Figure 1i represents a dendrite-free morphology on cycled anode equipped with VF separator, giving symmetric cell with ultra-long cycling life which exceeds most of the reported separators for symmetric cells (Figure 1j and Table S1). Zn

dendrites are found on the Zn anodes of cells equipped with GF and CF separators (Figure 1e, g), indicating their poor regulation in uniform Zn deposition. In this work, Zn foil was used as received, and its surface was microscopically uneven (Figure S13). Due to the tip effect, Zn crystals preferentially deposit on protrusions to form Zn dendrites.[46] The formation of loose dendrites on the surface of the Zn anode creates additional reactive sites, which results in HER and other side reactions. Moreover, the continuously growing dendrites penetrate the porous separators, ultimately causing a short circuit in the cells.[47] HER will lead to Zn anode corrosion and cell inflation, which are confirmed by the corrosion holes on the cycled anodes of cells equipped with GF and CF separators (Figure 1e, g) and the obvious increase in thickness of cycled symmetric cells (Figure 1k and Figure S14). Therefore, the uncontrolled dendrite growth and HER lead to the fast shorted circuits of symmetric cells equipped with GF and CF separators (Figure 1b). As anticipated, uniform Zn deposition without obvious HER is found on the Zn anode of the cell with a VF separator (Figure 1i, k), indicating the superior ability of VF in regulating Zn deposition.

Since profiled viscose rayons are regenerated from cotton fibers, the advantages of the VF separator over the CF separator in terms of Zn deposition and HER suppression can be attributed to the changes in chemical and microstructure caused by the cellulose regeneration process. On the one hand, it is well-known that the chemical structure of separators affects the electrolyte affinity and the desolvation of $[Zn(H_2O)_6]^{2+}$.[27] On the other hand, the reported literature suggested that functional groups on separators construct virtual pathways for Zn^{2+} transport,[48] which inspires us to deduce that the surface groove of profiled viscose rayon could probably provide a physically existing pathway for the transport of Zn^{2+}. Therefore, the chemical structure and micro-structure of CF and VF separators are characterized and compared.

Fourier transform infrared (FTIR) spectroscopy and X-ray photoelectron spectroscopy (XPS) were applied to analyse the difference in chemical structure of CF and VF (Figure 2a-e). As shown in Figure 2a, absorption bands at 3334 cm^{-1} and 1650 cm^{-1}, corresponding to the -OH and C=O stretching vibrations of cellulose, are found for both CF and VF separators. XPS analysis (Figure S15 and Table S2) reveals that the oxygen content of VF is higher than that of CF, probably due to the oxidation of primary hydroxyl groups to carboxyl groups. Figure 2b reveals that CF has the typical high-resolution XPS spectra for cellulose which can be decomposed into three peaks attributed to C-C/C-H (284.7 eV), C-O (286.5 eV), O-C-O/C=O (287.9 eV),[49] respectively. As cotton fibers (raw material for CF) are regenerated into viscose rayons (raw materials for VF), the decrease in the fraction of C-C/C-H and O-C-O/C=O bonds, along with the appearance of a new peak for O=C-O (Figure 2e) demonstrate the oxidation of primary hydroxyl groups and terminal aldehyde groups into carboxyl groups (Figure 2c). The broader absorption band at 3340 cm^{-1} for VF than that of CF (Figure 2a), attributed to the coordination between -OH and -COOH of VF, further supports the presence of carboxyl groups in the viscose structure.

Figure 2d shows FTIR spectra of CF and VF before and after being immersed in 2 M $ZnSO_4$ solution (electrolyte). For the VF separator, a distinct red-shift of the absorption peak at 3313 cm^{-1} is observed, revealing strong coordination between -COOH groups of VF and Zn^{2+}. However, there is no red shift was observed for CF separator, which indicates insufficient coordination between the -OH groups of CF and Zn^{2+}. Figure 2f, g shows the electrostatic potential (ESP) mapping of cellulose molecules for CF and viscose molecules for VF. Compared with the cellulose molecule, the viscose molecule exhibits more areas with low electronegativity, demonstrating a stronger coordination ability of the viscose molecule with Zn^{2+}. Fragments of cellulose molecule and viscose molecule (Figure S16) are applied to represent CF and VF, respectively, for density functional theory (DFT) calculations. Figure 2h shows that the binding energies of cellulose molecule of CF (-269.17 $kcal \cdot mol^{-1}$, Table S3) and viscose molecule of VF (-372.98 $kcal \cdot mol^{-1}$, Table S4) with Zn^{2+} are more negative than that of H_2O (-93.83 $kcal \cdot mol^{-1}$, Table S5) with Zn^{2+}, indicating that both CF and VF separators coordinate more favorably with Zn^{2+} than H_2O. Moreover, the binding energy of VF with Zn^{2+} is more than 100 $kcal \cdot mol^{-1}$ lower than that of CF, which, together with results from FTIR (Figure 2d) and ESP mapping (Figure 2f), reveals that VF has a much stronger coordination ability with Zn^{2+} than CF. Therefore, as $[Zn(H_2O)_6]^{2+}$ passes through the VF separator, the strong coordination between carboxyl groups on the VF surface and Zn^{2+} significantly promotes the desolvation process of $[Zn(H_2O)_6]^{2+}$, causing more H_2O molecules to be removed from $[Zn(H_2O)_6]^{2+}$.[3] Before Zn deposition, hydrated Zn^{2+} with fewer H_2O molecules or even bare Zn^{2+} reach the Zn anode and fewer active H_2O molecules are released, which significantly inhibits the water-induced side reactions (Figure 1i, k). In contrast, the poor desolvation ability of GF and CF separators on $[Zn(H_2O)_6]^{2+}$ leads to Zn^{2+} carrying more H_2O molecules to the Zn anode, triggering serious water-induced side reactions including hydrogen evolution (Figure 1k) and corrosion (Figure 1e, g). The enhanced ability of the VF separator to inhibit anode corrosion and HER is further demonstrated by the following electrochemical analyses. Linear polarization test (Figure 2i) shows that the VF separator possesses the lowest corrosion current density, indicating the best anti-corrosion ability. In AZIBs, Zn corrosion is primarily caused by HER. Linear sweep voltammetry (LSV) measurement (Figure 2j) indicates that VF separator can more effectively suppress HER activity than CF separator. After 40 cycles of stripping/plating, the XRD pattern of the Zn anode of the cell with CF separator (Figure 2k) shows distinct peaks at 8.52°, 17.16° and 25.86° corresponding to the corrosion byproduct ($Zn_4SO_4(OH)_6 \cdot 5H_2O$, PDF#00-039-0688), which almost completely disappears for Zn anode with VF separator, indicating the superior ability of the VF separator to suppress both HER and corrosion.

To investigate whether the ultra-long cycling lifespan and the alleviated HER are solely caused by the chemical structure of VF, an experiment is designed to verify the impact of introducing carboxyl groups merely onto the separator and its

effect on battery performance. CF is oxidized by TEMPO (2,2,6,6-Tetramethylpiperidin-1-oxyl) to introduce carboxyl

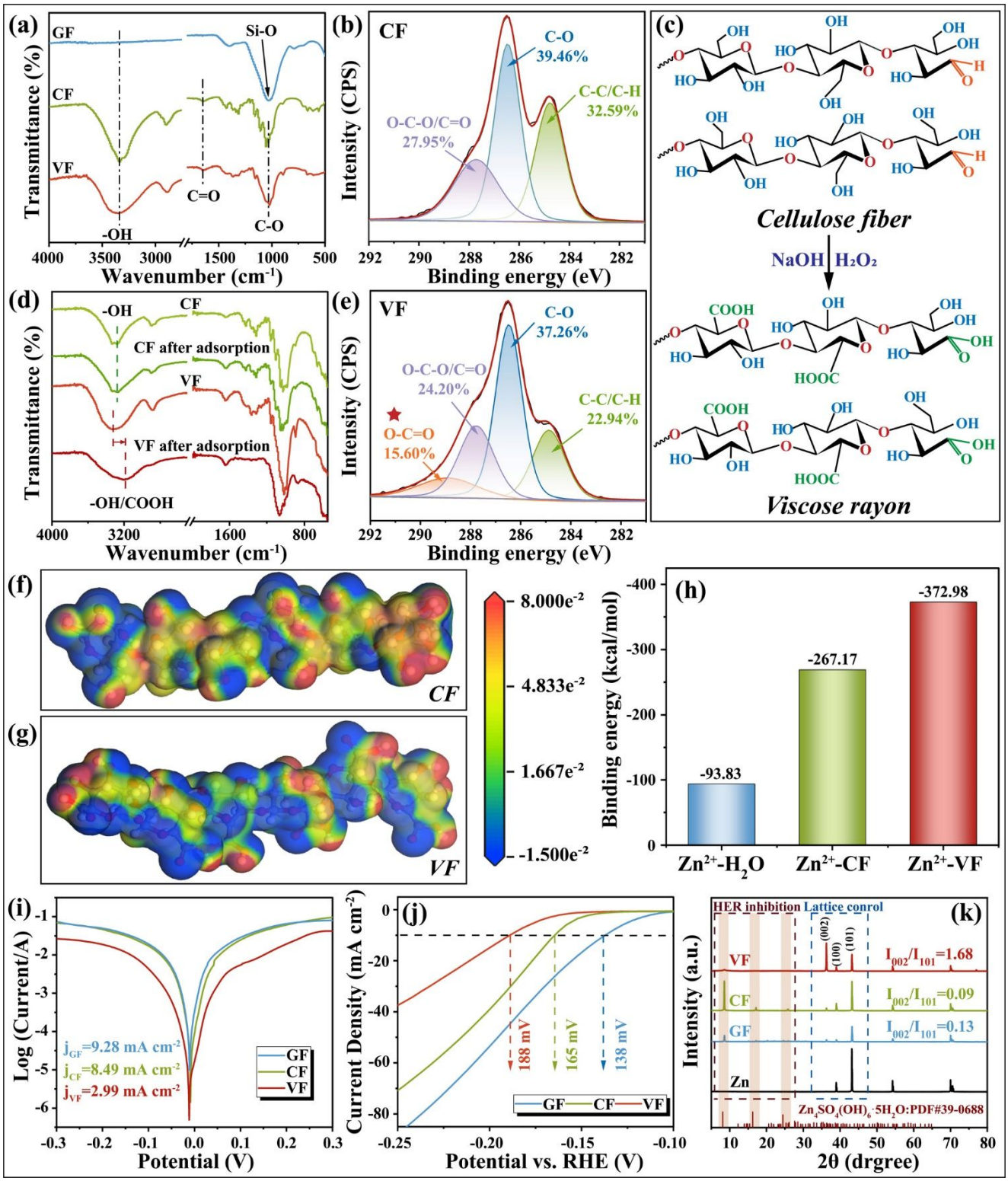

Figure 2. (a) FTIR spectra of GF, CF and VF separators and (d) FTIR red-shift of CF and VF after electrolyte adsorption. High-resolution XPS C1s spectra of (b) CF and (e) VF separators. (c) The oxidation process of cellulose into viscose during the production of viscose. ESP mapping of (f) CF and (g) VF. (h) The binding energies of Zn^{2+} to H_2O, CF and VF separators from DFT calculations (*see SI: 1.6 DFT calculations*). The (i) Tafel plots and (j) LSV curves of the cells with GF, CF and VF separators. (k) XRD spectra of Zn anodes from symmetric cells equipped with GF, CF and VF separators cycled for 40 cycles at 1 mA cm^{-2}.

groups onto the CF surface (Figure S17-19 and Table S6) without obvious change in surface morphology. Tafel and LSV curves of CF and oxidized-CF (Figure S20 and Figure S21) reveal that the introduction of carboxyl groups indeed significantly enhances the

ability of CF separator to suppress the anode corrosion and HER. However, the corrosion and HER resistance of TEMPO oxidized-CF are still not as good as those of the VF separator. The introduction of carboxyl groups onto CF also increases $\tau_{Zn^{2+}}$ (Figure S22), which is beneficial for the cycle stability of the battery. Accordingly, the cycle life of a symmetrical cell equipped with an oxidized CF separator has been extended to 105 h (Figure S23), which is 15 times that of a symmetric cell equipped with a pristine CF separator. However, this is still far below the 4600 h cycle life of the VF-equipped symmetric cell. This experiment indicates that carboxyl groups introduced during the cellulose regeneration process do not impart the VF separator with the ability to effectively regulate uniform Zn deposition. Therefore, the microstructural features imparted by the cellulose regeneration process also play a crucial role in modulating cell performance.

In the production process of viscose rayon, the spinning process includes two important processes: the salting-out solidification and the decomposition reaction of the cellulose xanthate.[50] During the salting-out solidification, the surface of the spinning fluid is firstly solidified into an outer layer of fiber (Figure 3a), and then the inner viscose fluid is slowly solidified. This imparts a skin-core structure to profiled viscose rayon, resulting in a serrated contour (Figure 3a), as the skin and core shrink at different rates. As shown in Figure 3b, the surface of the profiled viscose rayon exhibits longitudinal striated grooves. Additionally, the release of CS_2 during the decomposition process generates numerous pores in both the skin and core regions of profiled viscose rayon (Figure 3c-f). The abundant pores and surface grooves in the VF separator can be respectively regarded as reservoirs and transport canals for Zn^{2+}, playing important roles in regulating the transport and distribution of Zn^{2+} at the anode-electrolyte interface. The ionic conductivity (Figure 3g) was measured using electrochemical impedance spectroscopy (EIS) on SS||SS symmetric cells equipped with different separators. The GF separator possesses higher ionic conductivity than the CF separator owing to its high porosity and greater electrolyte uptake (Figure S2). However, the ionic conductivity of the VF separator is 4.4 times greater than that of the CF separator, probably owing to the higher Zn^{2+} transport rate through the surface grooves of profiled viscose rayon, which helps reduce the overpotential during Zn deposition.[51] According to the nucleation overpotential tests of Zn^{2+} (Figure 3h), the symmetric cell with a VF separator exhibits the lowest overpotential value of 64.70 mV, indicating the lowest nucleation barrier, which promotes the homogeneous Zn deposition (Figure 1i).[52] Chronoamperometry (CA) tests are performed to determine the Zn deposition manner. Zn symmetric cells with a fixed overpotential of -150 mV are used to record the CA curves. The polarization current of cell with CF separator increases rapidly over 300 s, indicating a continuous 2D diffusion process (Figure 3i) [53]. This leads to an uneven Zn deposition (Figure 1g) and the frantic Zn dendrites growth in the long-term cycling of cells (Figure 1d, f). In contrast, the polarization current increased rather slowly in the cell with VF separator. 2D diffusion process appears only in the first 16 s and then turns into a continuous 3D diffusion (Figure 3i). This indicates that VF realizes the uniformly distributed electric field on the Zn anode, which is very beneficial to the uniform Zn deposition (Figure 1i). Zn deposition manner is highly related to the Zn^{2+} transport rate.[12] The Zn^{2+} transference number ($\tau_{Zn^{2+}}$) in Zn symmetric cells was determined by potentiostatic direct-current polarization to examine the regulation effect of separators on ion transport. As shown in Figure 3j and Figure S24, $\tau_{Zn^{2+}}$ of symmetric cells equipped with VF separator (0.61) was two times as high as that of cells with CF separator (0.30) and GF separator (0.29). The electrochemical properties discussed above for GF, CF, VF, FP and BF separators are presented in Figure S24-27. A comprehensive comparison of these five separators in terms of physical properties, electrochemical properties, price, etc., is summarized in Table S7, highlighting the advantage of VF as a separator in AZIBs.

The electrochemical performance discussed above has proven that VF separator has achieved faster Zn^{2+} transport and uniform Zn^{2+} distribution, which is probably attributed to the spontaneous capillary action of surface grooves on profiled viscose rayon in the VF separator. To demonstrate the role of surface grooves on profiled viscose rayon in accelerating Zn^{2+} transport, finite element analysis is performed to calculate the diffusion process of Zn^{2+} within cotton fiber (for CF separator) and profiled viscose rayon (for VF separator), respectively. The cylindrical models with and without surface longitudinally striated grooves are built for them, as shown in Figure S28, and the diameter and length of them are 15 and 30 μm, respectively. The hydration of Zn^{2+} is realized by introducing the interfacial reaction rate between Zn^{2+} and fibers surface. Then, the diffusion of hydrated Zn^{2+} within the fibers is modeled utilizing the dilute species transport module, where the adsorption interactions of the fibers with Zn^{2+} and SO_4^{2-} are considered (Equation (1)). Finally, the fluid motion is described using the Nernst-Planck equation (Equation (2)).

$$R_s = -D\frac{\partial c_i}{\partial n} \quad (1)$$

$$\frac{\partial c_i}{\partial t} + \nabla \cdot (-D_i \nabla c_i) = 0 \quad (2)$$

where R_s represents the adsorption rate of Zn^{2+} and SO_4^{2-} on the surface of profiled viscose rayon and cotton fiber, and n refers to the direction perpendicular to the interface. c_i and D_i denote the ion concentration and the ion diffusion coefficient, respectively. The 2 M $ZnSO_4$ solution is set based on an experimental sample with $D_{Zn^{2+}} = 0.703 \times 10^{-9} m^{-2} s^{-1}$ and $D_{SO_4^{2-}} = 1.065 \times 10^{-9} m^{-2} s^{-1}$. Initially, the concentration at the boundary condition of the left is set as 2 M while the right boundary condition is set as an outflow boundary. The surface reaction of the fibers with Zn^{2+} and SO_4^{2-} is established, with an initial concentration set to zero. The mesh numbers of cotton fabric and profiled viscose rayon were tested, with their converged mesh number determined to be 98987 and 140986, respectively. The flow of 2 M $ZnSO_4$ is applied from the left side of fibers to achieve the concentration profile of hydrated Zn^{2+} concerning diffusion time in the 1D fiber models (Figure 3k, l). A striking difference in the diffusion efficiency of hydrated Zn^{2+} between cotton fiber and profiled viscose rayon is found, even within a short period of 35 cs, with a significantly enhanced mass transfer of Zn^{2+} in profiled viscose rayon due to the presence of surface grooves. Specifically, the concentration evolution of Zn^{2+}

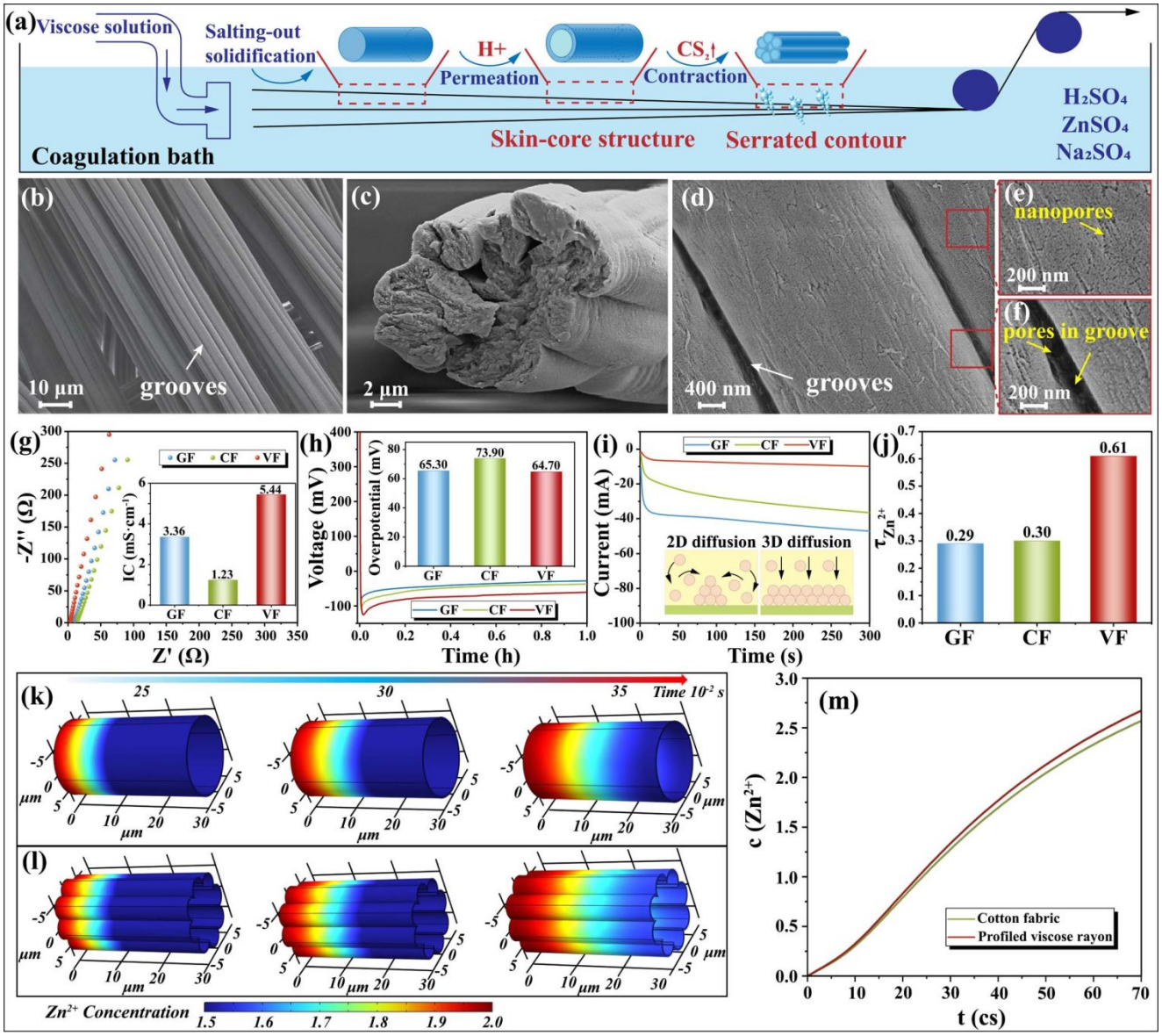

Figure 3. (a) Wet spinning process of commercial profiled viscose rayon. SEM images of VF separator: (b) longitudinally striated grooves, (c) cross-section and (d, e, f) nano-pores in the skin and micron-pores in the grooves. (g) The EIS curves in the SS||SS symmetric cells with different separators; the inset presents the ionic conductivities (IC) of the separators. (h) The voltage-time profiles of the cell with GF, CF and VF separators at 0.5 mA cm^{-2}. (i) Chronoamperometry (CA) test of the cell with GF, CF and VF separators under -150 mV. (j) Zn^{2+} transference number ($\tau_{Zn^{2+}}$) of different separators. Concentration profile of Zn^{2+} through the surface of (k) cotton fiber and (l) profiled viscose rayon obtained by finite element simulation along the time of 1 to 35 cs. (m) Concentration evolution of one position on cotton fiber and profiled viscose rayon.

further signifies the importance of surface grooves on profiled viscose rayon in enhanced mass transfer of Zn^{2+} (Figure 3m).

To investigate the role of surface grooves on profiled viscose rayon in regulating Zn^{2+} transport and promoting uniform Zn deposition, two comparative experiments are designed. The first experiment involves tearing and reconstituting profiled viscose rayon into a membrane (named G-VF) with a similar weight per unit area as VF by grinding and suction filtration. Figure S29 shows that the colloid mill severely disrupts the original surface grooves of the viscose rayons, resulting in a significant decrease in $\tau_{Zn^{2+}}$ from 0.61 to 0.37 (Figure S30). Correspondingly, the G-VF without surface grooves losts the ability to regulate the growth of Zn crystals along the (002) plane on the anode surface and to facilitate uniform Zn deposition (Figure S31), causing the symmetric cell cycle life to drop to only 37 h (Figure S32). In the second experiment (see *SI: Preparation and characterization of VF@SiO_2*), profiled viscose rayons in the VF separator are well-covered by a layer of hydrophilic SiO_2 nanoparticles (Figure S33), and the modified VF separator is named as VF@SiO_2. With the surface grooves on the profiled viscose rayons covered by SiO_2 nanoparticles, $\tau_{Zn^{2+}}$ value and cycle life of symmetric cells with VF@SiO_2 separator are reduced to 0.43 and 60 h, respectively (Figure S34 and Figure S35). Additionally, Figure S36 shows non-uniform Zn deposition and the preferential growth of the (101) crystal plane of Zn. These two experiments demonstrate the crucial role of the surface grooves on profiled viscose rayons in accelerating the Zn^{2+} transport rate for long-term AZIBs.

The effect of CF, VF and GF separators on the regulation of Zn growth manner is compared by SEM images of their Zn electrodes cycled for 10 s, 30 s, 5 min, 30 min and 100 h, respectively (Figure 4a-f, Figure S37-41). In the initial stage of charging, the loose CF and VF separators allow amounts of Zn^{2+} to quickly pass through the pores of separators to reach the Zn anode and then a fast Zn deposition along the (101) orientation is observed.[26, 31] Figure 4g-i, illustrates the schematic diagram of the regulation of Zn^{2+} distribution at the anode-electrolyte interface by CF separator and Zn plating process. Due to the inevitable unevenness on the surface of Zn foil, the electric field at the protrusion is strengthened,[54] and a large number of Zn^{2+} are attracted from the adjacent place to the

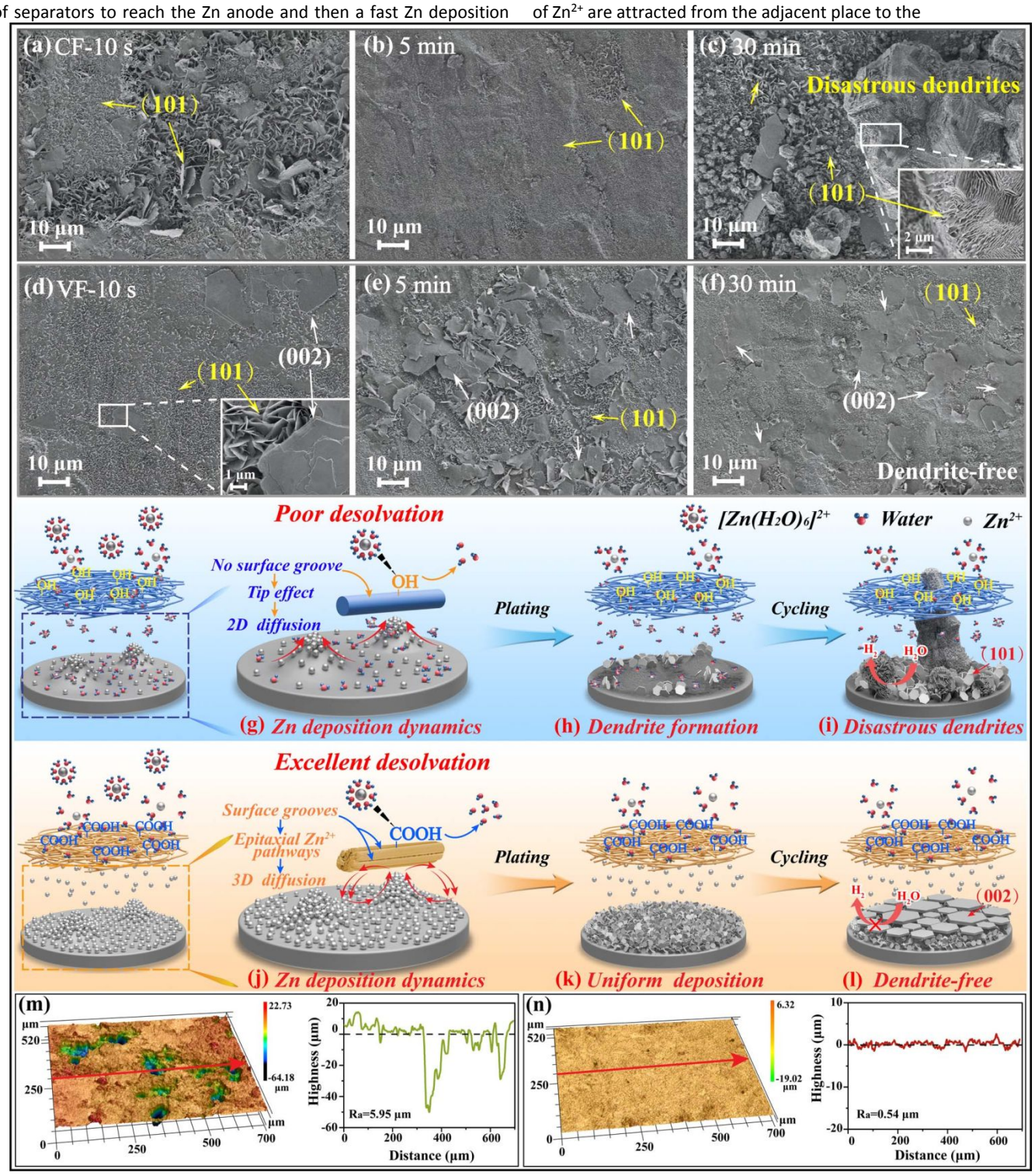

Figure 4. SEM images of Zn anode after deposition for 10 s, 5 min and 30 min with (a, b, c) CF and (d, e, f) VF separators at 0.5 mA cm^{-2}. Schematic of Zn plating behavior on Zn anodes with (g-i) CF separator and (j-l) VF separator. CLSM images with the corresponding surface roughness curve of Zn anode after deposition for 100 h with (m) CF and (n) VF separators.

protrusion (Figure 4g). The Zn deposition rate on the protuberance is much higher than on the adjacent sites (tip-effect).[55] For the cell equipped with a CF separator, due to the sluggish Zn^{2+} transport at the electrolyte/anode interface (Figure 3j), the continuous growth of Zn crystals can no longer attract Zn^{2+} from their adjacent Zn^{2+}-deficient areas (Figure 4g). At this stage, most Zn^{2+} ions are replenished from the electrolyte above the Zn crystals, resulting in the formation of a thick Zn^{2+} diffusion layer. This means that during Zn deposition, Zn^{2+} diffuses in a 2D manner, leading to the vertical growth of Zn crystals. This is convincingly verified by the XRD spectrum of cycled Zn anode with CF separator, in which the intensity ratio of the diffraction peaks of Zn (002)/ (101) is only 0.09 (Figure 2k). This suggests that with the 2D diffusion manner, a tiny protrusion (Figure 4a, h) can rapidly evolve into a disastrous dendrite (as shown in Figure 4c, i). SEM images of cycled anodes at different times also indicate a continued 2D diffusion of Zn^{2+} for cells equipped with CF separator throughout the plating process, which is in good agreement with the CA test results in Figure 3i. For cycled Zn anode with VF separator, even after being cycled for only 10 s, many Zn crystals growing along the (002) direction are found on the top of (101) Zn crystals (Figure 4d-f), which indicates that the surface grooves on profiled viscose rayons in VF have excellent capability in lattice control during Zn deposition. Figure 4j-l, illustrates the schematic diagram of the regulation of Zn^{2+} distribution at the anode-electrolyte interface by VF separator and Zn plating process. As shown in Figure 4k, similar to the cell with CF separator, amounts of Zn plates also formed along the (101) direction on Zn anode of cell with VF separator at the beginning of charging. If this manner continues, Zn^{2+} will also tend to accumulate on the protuberances to form an inhomogeneous Zn^{2+} distribution. Fortunately, most of the profiled viscose rayons in the VF separator are parallel to the Zn anode (Figure 1a and Figure 3b). As shown in Figure 4j, the surface grooves on profiled viscose rayons provide amounts of epitaxial pathways for rapid horizontal transport of Zn^{2+} at the electrolyte/anode interface, which brings two advantages to the Zn deposition dynamic. Firstly, it helps to eliminate the tip effect, as Zn^{2+} ions, which would otherwise accumulate due to the

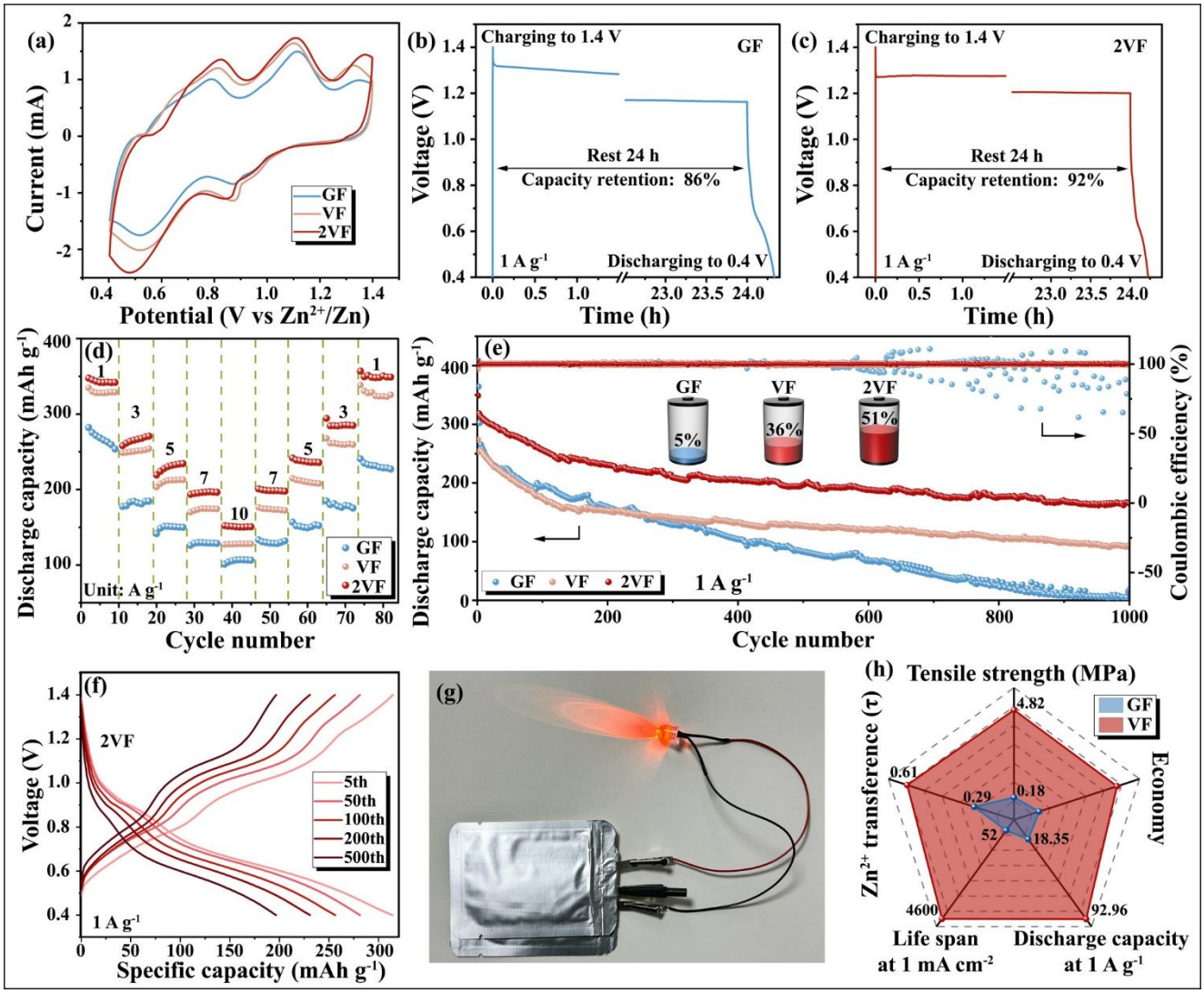

Figure 5. Electrochemical performance of Zn||NVO with GF, VF and 2VF separators. (a) CV curves at 1 mV/s. (b-c) Self-discharge measurements at 1 A g^{-1}. (d) Rate performance. (e) Cycle stability at 1 A g^{-1}. (f) Charge/discharge curves at 1 A g^{-1}. (g) Digital photograph of two assembled Zn|VF|NVO pouch cells in series powered for a red indicator light. (h) The radar chart for different comparisons of GF and VF separators.

tip effect, are rapidly redirected horizontally to the adjacent Zn^{2+}-deficient regions (Figure 4j). This mechanism leads to a highly uniform distribution of Zn^{2+} across the surface of the Zn anode. Secondly, the rapid horizontal transport of Zn^{2+} prevents the replenishment of Zn^{2+} from the electrolyte in the vertical direction, thus significantly reducing the thickness of the diffusion layer. Therefore, the diffusion behavior of Zn^{2+} shifts from a 2D mode to a 3D mode (Figure 3i). During the growth of Zn crystals, the replenishment of Zn^{2+} from the horizontal direction enables the epitaxial growth of Zn crystals along the (002) plane (Figure 4l). This phenomenon had been observed by Archer et al.[56] The XRD results (Figure 2k) reveal that the intensity ratio of the diffraction peaks between Zn (002) and (101) for the cycled electrode with VF separator is 1.68, much higher than that of CF (0.09) and GF (0.13) separators. Initially, a short 2D diffusion forms a uniform deposition of small Zn anode along the (101) direction over a brief period (Figure 3i and Figure 4d). Later, a continuous 3D diffusion forms the epitaxial growth of the Zn anode along the (002) direction on the top of the (101) Zn anode (Figure 4d-f and Figure S42). Figure S42 also shows that the (002) Zn anode originates from the profiled viscose rayon, demonstrating the role of the profiled viscose rayon in the reconfiguring of Zn deposition. Meanwhile, the batteries equipped with VF separators were disassembled after the 1st, 5th, 50th and 100th cycles respectively, and the XRD patterns of the anodes were recorded as shown in Figure S43. The intensity ratio of the diffraction peaks of Zn (002) and Zn (101) gradually increased from 0.22 to 2.13, which proved that the Zn deposition on the anode through the VF separator continued in an epitaxial growth manner. In addition, Figure 4g-j also depicts the desolvation process of the $[Zn(H_2O)_6]^{2+}$ through CF or VF, as well as HER on the anode surface, as previously described. Finally, confocal laser scanning microscopy (CLSM) was employed to show the 3D morphology of Zn anodes cycled for 100 h. For the cell equipped with CF separator, Zn anode exhibits an uneven morphology of *mountain-lake landform* with an average surface roughness of 5.95 μm (Figure 4m), in which the *lakes* are induced by the Zn corrosion and the *mountains* are formed by the dendrite growth. In contrast, for the cell with VF separator, Zn anode shows a flat surface without *mountain* and *lake*, and the average surface roughness is only 0.54 μm (Figure 4n), revealing the advantages of VF separator in inhibiting dendrite growth and HER. Therefore, the VF separator can efficiently enhance the reversibility of Zn anodes (Figures 1c and S11).

To verify the practicability of VF separator in AZIBs, Zn||NVO full battery with one layer of VF (labeled as VF) and two layers of VF (labeled as 2VF) were respectively assembled and compared with that of commercial GF separator. $NH_4V_4O_{10}$ (NVO) was prepared by hydrothermal method (see *SI: Preparation and characterization of $NH_4V_4O_{10}$*, Figure S44). The CV curves of Zn||NVO full cell equipped with VF and 2VF separators show the same redox peaks as that of cell with GF separator (Figure 5a). However, full cells with VF and 2VF separators have larger peak currents, indicating that they have higher electrochemical activity, higher capacity and better battery performance. Moreover, the EIS results show that the Zn|VF|NVO and Zn|2VF|NVO exhibit lower charge transfer resistance compared to the Zn|GF|NVO, indicating lower ion transference impedance and enhanced Zn^{2+} diffusion kinetics (Figure S45). To evaluate the effectiveness of the VF and 2VF separators in reducing self-discharge behavior, a 24 h self-discharging test was conducted (Figure 5b, c, and Figure S46). Following a 24 h resting period, the Zn||NVO cell equipped with the 2VF separator shows an improved capacitance retention of 92%, surpassing that of GF separator (86%). Figure 5d shows that full cells equipped with VF and 2VF separators possess better rate capability. When the current density returns to 1 A g^{-1}, the specific discharge capacity of Zn|2VF|NVO and Zn|VF|NVO full cell can be recovered by 100% and 99.14%, while it can only recovered by 86.68% for Zn|GF|NVO full cell, indicating the excellent reversibility of VF equipped cells. Figure 5e, f and Figure S47-48 show that VF separator also endows Zn||NVO full cell with much better long-term cycling performance. Zn|2VF|NVO full cell delivers a discharge capacity of 165.29 mAh g^{-1} and possesses capacity retention of 51.25% after 1000 cycles, which are significantly higher than those of cells with GF separator (18.25 mAh g^{-1} discharge capacity and 5.01% capacity retention). The pouch cell assembled with a viscose separator can power an LED light (Figure 5g). Its cycle stability and energy density are discussed in the *Supporting Information* (Figure S49). Finally, the advantages of VF separator to commercial GF separator as well as FP, CF and BF separators are presented in Figure 5h and Table S7.

Conclusions

In summary, we have developed an ultra-low-cost commercial non-woven VF separator, derived from profiled viscose rayon, to stabilize the Zn anode of AZIBs. Profiled viscose rayons contain abundant carboxyl groups and surface grooves, which reconfigure the interface dynamics of Zn deposition. Carboxyl groups facilitate the desolvation of hydrated Zn^{2+}, reducing the corrosion current density and suppressing the HER activity. Surface grooves provide epitaxial pathways for rapid Zn^{2+} transport at the electrolyte/anode interface, promoting the fast transition of Zn deposition from 2D diffusion to 3D diffusion, endowing VF separator with excellent ability to regulate the growth direction of Zn crystals from (101) to (002) for a uniform and dense Zn deposition on Zn anode. Accordingly, Zn symmetric cell with VF separator reveals ultra-long cycling performance (over 4600 h at 1 mA cm^{-2}), significantly higher than those of GF and CF separators (52 h and 7 h). Additionally, the NVO|2VF|Zn full battery exhibits a higher discharge capacity (165.29 mAh g^{-1}) and capacity retention (51.25%) than battery equipped with GF separator (18.25 mAh g^{-1} and 5.01%) at 1 A g^{-1} after 1000 cycles. This work highlights the benefits of profiled fibers in regulating the electrochemical performance of AZIBs and offers a new approach to designing innovative separators.

Author contributions

S. Ou designed and performed the research on material synthesis, data analysis and manuscript writing. J. Zheng contributed to the pouch cell assembly, data analysis and manuscript revision. X. Chen and R. Li contributed to the electrochemical measurements, FTIR and XPS measurements and analysis. Y. Niu and M. An contributed to finite element analysis. G. Zhou contributed to molecular dynamics simulation. S. Liu, Z. Yuan, Y. Yamauchi and X. Zhang developed the

idea for the study. All the authors contributed to the writing and revisions.

Conflicts of interest

The authors declare no conflict of interest.

Data availability

The data that support the findings of this study are available from the corresponding author upon reasonable request.

Acknowledgements

This work was partially supported by the Forestry Science and Technology Project of Fujian Province of China (No.2023FKJ27), Department of Science and Technology of Fujian Province of China (No.2022H6021), National Natural Science Foundation of China (No.52302223), the ARC Laureate Fellowship (FL230100095) and the JST-ERATO Yamauchi Materials Space Tectonics Project (JPMJER2003). This work used the Queensland node of the NCRIS-enabled Australian National Fabrication Facility (ANFF).

References

1. J. Wan, R. Wang, Z. Liu, S. Zhang, J. Hao, J. Mao, H. Li, D. Chao, L. Zhang, C. Zhang, *Adv. Mater.* **2024**, *36*, 2310623.
2. C. Nie, G. Wang, D. Wang, M. Wang, X. Gao, Z. Bai, N. Wang, J. Yang, Z. Xing, S. Dou, *Adv. Energy Mater.* **2023**, *13*, 2300606.
3. Y. Zong, H. He, Y. Wang, M. Wu, X. Ren, Z. Bai, N. Wang, X. Ning, S. Dou, *Adv. Energy Mater.* **2023**, *13*, 2300403.
4. W. Ma, S. Wang, X. Wu, W. Liu, F. Yang, S. Liu, S.C. Jun, L. Dai, Z. He, Q. Zhang, *Energy Environ. Sci.* **2024**, *17*, 4819-4846.
5. W. Sun, F. Wang, B. Zhang, M. Zhang, V. Küpers, X. Ji, C. Theile, P. Bieker, K. Xu, C. Wang, M. Winter, *Science* **2021**, *371*, 46-51.
6. Y. Mu, Z. Li, B. Wu, H. Huang, F. Wu, Y. Chu, L. Zou, M. Yang, J. He, L. Ye, M. Han, T. Zhao, L. Zeng, *Nat. Commun.* **2023**, *14*, 4205.
7. S. Yang, A. Chen, Z. Tang, Z. Wu, P. Li, Y. Wang, X. Wang, X. Jin, S. Bai, C. Zhi, *Energy Environ. Sci.* **2024**, *17*, 1095-1106.
8. J. Cao, Y. Sun, D. Zhang, D. Luo, L. Zhang, R. Chanajaree, J. Qin, X. Yang, J. Lu, *Adv. Energy Mater.* **2024**, *14*, 230770.
9. Q. He, Z. Chang, Y. Zhong, S. Chai, C. Fu, S. Liang, G. Fang, A. Pan, *ACS Energy Lett.* **2023**, *8*, 5253-5263.
10. L. Han, Q. Wang, R. Pang, D. Zhang, B. Zhao, W. Meng, M. Li, Y. Zhang, A. Cao, Y. Shang, *Adv. Energy Mater.* **2023**, *13*, 2302395.
11. M. Liu, C. Tian, D. Zhang, Y. Zhang, B. Zhang, Y. Wang, C. Li, M. Liu, B. Gu, K. Zhao, L. Kong, Y Chueh, *Nano Energy* **2022**, *103*, 107805.
12. Z. Shi, M. Yang, Y. Ren, Y. Wang, J. Guo, J. Yin, F. Lai, W. Zhang, S. Chen, H. Alshareef, T. Liu, *ACS Nano* **2023**, *17*, 21893-21904.
13. Q. Wang, J. Zhao, J. Zhang, M. Li, F. Tan, X. Xue, Z. Sui, Y. Zou, X. Zhang, W. Zhang, C. Lu, *Adv. Funct. Mater.* **2024**, *34*, 2405957.
14. F. Shen, H. Du, H. Qin, Z. Wei, W. Kuang, N. Hu, W. Lv, Z. Yi, D. Huang, Z. Chen, H. He, *Small.* **2024**, *20*, 2305119.
15. H. Ma, J. Yu, M. Chen, X. Han, J. Chen, B. Liu, S. Shi, *Adv. Funct. Mater.* **2023**, *33*, 2307384.
16. Z. Luo, L. Ren, Y. Chen, Y. Zhao, Y. Huyan, Z. Hou, J. Wang. *Chem. Eng. J.* **2024**, *481*, 148448.
17. X. Yang, W. Li, J. Lv, G. Sun, Z. Shi, Y. Su, X. Lian, Y. Shao, A. Zhi, X. Tian, X. Bai, Z.Liu, J. Sun, *Nano Res.* **2022**, *15*, 9785-9791.
18. Y. Su, B. Liu, Q. Zhang, J. Peng, C. Wei, S. Li, W. Li, Z. Xue, X. Yang, J. Sun, *Adv. Funct. Mater.* **2022**, *32*, 2204306.
19. F. Wu, F. Du, P. Ruan, G. Cai, Y. Chen, X. Yin, L. Ma, R. Yin, W. Shi, W. Liu, J. Zhou, X. Cao, *J. Mater. Chem. A* **2023**, *11*, 11254-11263.
20. X. Yang, W. Wu, Y. Liu, Z. Lin, X. Sun, *Chem. Eng. J.* **2022**, *450*, 137902.
21. D. Zhu, Y. Guo, J. Ren, MA. Abu-Tahon, SM. El-Bahy, H. Song, Y. Liu, F. Ren, ZM. El-Bahy, *Adv. Compos. Hybrid. Mater.* **2024**, *7*, 205.
22. S. Yang, Y. Zhang, Y. Zhang, J. Deng, N. Chen, S. Xie, Y. Ma, Z. Wang, *Adv. Funct. Mater.* **2023**, *33*, 2304280.
23. Y. Li, X. Peng, X. Li, L. Dong, F. Kang, *Adv. Mater.* **2023**, *35*, 2300019.
24. Y. Zhang, Z. Liu, X. Li, L. Fan, Y. Shuai, N. Zhang, *Adv. Energy Mater.* **2023**, *13*, 2302126.
25. J. Cao, D. Zhang, C. Gu, X. Zhang, M. Okhawilai, S. Wang, J. Han, J. Qin, Y. Huang, *Nano Energy* **2021**, *89*, 106322.
26. J. Cao, D. Zhang, C. Gu, X. Wang, S. Wang, X. Zhang, J. Qin, Z. Wu, *Adv. Energy Mater.* **2021**, *11*, 2101299.
27. Y. Fang, X. Xie, B. Zhang, Y. Chai, B. Lu, M. Liu, J. Zhou, S. Liang, *Adv. Funct. Mater.* **2022**, *32*, 2109671.
28. L. Yao, C. Hou, M. Liu, H. Chen, Q. Zhao, Y. Zhao, Y. Wang, L. Liu, Z. Yin, J. Qiu, *Adv. Funct. Mater.* **2023**, *33*, 2209301.
29. B. Wu, Y. Wu, Z. Lu, J. Zhang, N. Han, Y. Wang, X. Li, M. Lin, L. Zeng, J. *Mater. Chem. A* **2021**, *9*, 4734-4743.
30. D.J. Arnot, M.B. Lim, N.S. Bell, N.B. Schorr, R.C. Hill, A. Meyer, Y. Cheng, T.N. Lambert, *Adv. Energy Mater.* **2021**, *11*, 2101594.
31. Y. An, Y. Tian, Q. Man, H. Shen, C. Liu, Y. Qian, S. Xiong, J. Feng, Y. Qian, *ACS Nano* **2022**, *16*, 6755-6770.
32. Y. Qin, P. Liu, Q. Zhang, Q. Wang, D. Sun, Y. Tang, Y. Ren, H. Wang, *Small* **2020**, *16*, 2003106.
33. Z. Li, X. Wu, X. Yu, S. Zhou, Y. Qiao, H. Zhou, S. Sun, *Nano Lett.* **2022**, *22*, 2538-2546.
34. Z. Li, L. Ye, G. Zhou, W. Xu, K. Zhao, X. Zhang, S. Hong, T. Ma, M. Li, C. Liu, C. Mei, *Chem. Eng. J.* **2023**, *457*, 141160.
35. W. Zhou, M. Chen, Q. Tian, J. Chen, X. Xu, C. Wong, *Energy Storage Mater.* **2022**, *44*, 57-65.
36. R. Chen, G. Zhang, H. Zhou, J. Li, J. Li, L. Chung, X. Hu, J. He, *Small* **2024**, *20*, 2305687.
37. LF. Zemljic , Z. Persin, P. Stenius, KS. Kleinschek, *Cellulose* **2008**, *15*, 681-690.
38. T. Genco, LF. Zemljic, M. Bracic, K. Stana-Kleinschek, T. Heinze T, *Cellulose* **2012**, *19*, 2057-2067.
39. C. Li, L. Li, J. Li, X. Wu, L. Qi, W. Li, *Cellulose* **2019**, *26*, 1631-1640.
40. C. Liu, Y. Wang, H. Liu, Q. Chen, X. Jiang, H. Jia, J. Lang, *Compos. Part B: Eng.* **2024**, *272,* 111227.
41. W. Tu, S. Liang, L. Song, X. Wang, G. Ji, J. Xu, *Adv. Funct. Mater.* **2024**, *34*, 2316137.
42. H. Qin, W. Chen, W. Kuang, N. Hu, X. Zhang, H. Weng, H. Tang, D. Huang, J. Xu, H. He, *Small* **2023**, *19*, 2300130.
43. M. Zhao, J. Rong, F. Huo, Y. Lv, B. Yue, Y. Xiao, Y. Chen, G. Hou, J. Qiu, S. Chen, Adv. Mater. **2022**, 34, 2203153.
44. S. Chen, K. Ouyang, Y. Liu, M. Cui, G. Pu, Y. Wang, K. Zhang, Y. Huang, *Angew. Chem. Int. Ed.* **2024**, 63, e202409303.
45. C. Zhu, P. Li, G. Xu, H. Cheng, G. Gao, Coord. *Chem. Rev.* **2023**, *485*, 215142.
46. Z. Tao, X. He, L. Yu, X. Ma, N. Ahmad, G. Zhang, *Small Methods* **2024**, *8*, 2400463.
47. T. Mageto, S.D. Bhoyate, K. Mensah-Darkwa, A. Kumar, R.K. Gupta, *J. Energy Storage* **2023**, *70*, 108081.

48. Y. Song, P. Ruan, C. Mao, Y. Chang, L. Wang, L. Dai, P. Zhou, B. Lu, J. Zhou, Z. He, *Nano-Micro Lett.* **2022**, *14*, 218.
49. Z. Liu, J. Yu, W. Lin, W. Yang, R. Li, H. Chen, X. Zhang, *Surf. Coat. Tech.* **2018**, *352*, 313-319.
50. I.S.F. Mendes, A. Prates, DV. Evtuguin, *Carbohydr. Polym.* **2021**, *273*, 118466.
51. Y. Chen, Z. Deng, Y. Sun, Y. Li, H. Zhang, G. Li, H. Zeng, X. Wang, *Nano-Micro Lett.* **2024**, *16*, 96.
52. S. Chen, J. Chen, X. Liao, Y. Li, W. Wang, R. Huang, T. Zhao, S. Yan, Z. Yan, F. Cheng, H. Wang, *ACS Energy Lett.* **2022**, *7*, 4028-4035.
53. Z. Liu, X Li, Z. Li, L. Ma, Y. Wang, C. Ye, M. Ye, J. Shen, *Chem. Eng. J.* **2024**, *479*, 147412.
54. Y. Gong, B. Wang, H, Ren, D. Li, D. Wang, H. Liu, S. Dou, *Nano-Micro Lett.* **2023**, *15*, 208.
55. Y. Zhang, X. Zheng, N. Wang, W. Lai, Y. Liu, S. Chou, H. Liu, S. Dou, Y. Wang, *Chem. Sci*. **2022**, *13*, 14246-14263.
56. J. Zheng, J. Yin, D. Zhang, G.Li, D.C. Bock, T. Tang, Q. Zhan, X. Liu, A. Warren, Y. Deng, S. Jin, A.C. Marschilok, E.S. Takeuchi, K.J. Takeuchi, C.D. Rahn,, L.A. Archer, Sci. Adv. **2020**, 6, eabb1122.

Data Availability Statement

The data that support the findings of this study are available from the corresponding author upon reasonable request.